Spectroscopic investigations of infrared-radiofluorescence (IR-RF) for equivalent dose estimation

Mariana Sontag-González[a*], Markus Fuchs[a]

[a] Department of Geography, Justus Liebig University, Giessen, Germany

* Corresponding author: Mariana.Sontag-Gonzalez@geogr.uni-giessen.de

Abstract

Infrared radiofluorescence (IR-RF) is a technique with the potential to date sediment deposition beyond 1000 Gy. However, the total IR-RF signal is composed of several emissions whose separate characteristics are still poorly understood. We obtained RF emission spectra for two sediment samples dominated by K-feldspar in the wavelengths ~600–1000 nm over a wide dose range of up to 4000 Gy to discuss possible effects of neighbouring emissions on the conventional IR-RF D_e estimation via a photomultiplier tube, which yields a signal integration over a wavelength range of more than 30–40 nm. The studied samples included a modern age and a field-saturated one to assess the emissions' characteristics at different dose ranges. For these samples, we find no significant influence of neighbouring emissions to the D_e obtained from the wavelength range typically used for IR-RF.

Keywords: Radiofluorescence; IR-RF; Spectroscopy; K-feldspar; Luminescence dating; QEMSCAN

1. Introduction

Radiofluorescence (RF) is the luminescence occurring during exposure of a mineral to ionizing radiation. The infrared (IR) RF emission of potassium (K) feldspar can be used as a dating technique to establish the time since sediment deposition (Trautmann et al., 1998, 1999a, 1999b). This technique has two main advantages over other common luminescence-based dating techniques: a datable range an order of magnitude higher than that of the optically stimulated luminescence of quartz and a higher signal stability (i.e., no loss of signal due to the

https://doi.org/10.1016/j.radmeas.2022.106733

phenomenon of ‘anomalous fading’) than the infrared stimulated luminescence of K-feldspar (e.g., Murari et al., 2021b). However, determination of IR-RF ages from samples with independent age controls has had only mixed success (e.g., Degering and Krbetschek, 2007; Wagner et al., 2010; Buylaert et al., 2012; Frouin et al., 2017; Kreutzer et al., 2018; Murari et al., 2021a). Potential reasons for this include insufficient correction for sensitivity changes, sample-specific signal instability or interference between different RF signals. Investigation of the latter possibility is the focus of this work.

Whereas the IR-RF signal obtained from the ~1.43 eV (865 nm) emission is broadly reported to be thermally and athermally stable, based on laboratory experiments (e.g., Krbetschek et al., 2000; Trautmann et al., 2000; Frouin et al., 2017) and successful dating of Middle Pleistocene age deposits (e.g., Wagner et al., 2010), there is a known possibility of a small but not insignificant signal contribution from neighbouring emissions at both higher and lower wavelengths, i.e., further into the IR and at red wavelengths. The latter is reportedly unstable (Trautmann et al., 1998; Krbetschek et al., 2000), so special consideration should be given to its possible overlap with the main IR-RF peak.

Trautmann et al. (1998) identified such red RF peaks in five feldspar samples of different mineralogy with variable signal intensity in comparison with other RF peaks in the IR to UV range. Unlike the IR-RF emission, the red emission signal grows with increasing dose (Trautmann et al., 1998; Krbetschek et al., 2000; Schilles, 2002; Erfurt and Krbetschek, 2003). By fitting the RF spectrum of a laboratory-dosed K-feldspar sample (500 Gy additive dose), Krbetschek et al. (2000) showed that the tail of the red emission centred at ~1.77 eV (700 nm) extends at least until 1.38 eV (900 nm) and, so, would be picked up in IR-RF measurements targeting the main IR emission. Similar observations were made by Schilles (2002), who added that the characteristics of the red RF emission peak can be sample-dependent, with relatively high variability between four K-feldspar samples: fitting with Gaussian functions yielded peak centres ranging 1.65–1.73 eV (751–717 nm) and standard deviations ranging 0.04–0.13 eV (the IR-RF peaks of these samples were somewhat narrower, ranging 0.03–0.07 eV). Part of this variability might arise from the presence of not only one, but two overlapping red RF emission peaks, at 1.68 and 1.77 eV (738 and 700 nm, respectively), as suggested by fitting RF spectra measured at 7 K of one K-feldspar sample (Kumar et al., 2018).

There can also be a signal overlap of the targeted IR emission with one of longer wavelength. While such an emission was first described by Erfurt and Krbetschek (2003) centred on 910 nm (1.36 eV) to improve the fit quality of a broad asymmetric peak in the IR range of their RF spectra, subsequent measurements at 7 K (where peaks are narrower) have

confirmed its presence and described its dose response as being very similar to that of the main IR-RF emission (Kumar et al., 2018; Riedesel et al., 2021). The seven low-temperature K-feldspar samples measured in these studies display a range of peak positions and widths. The emission peaks described by Erfurt and Krbetschek (2003) as being centred at 1.43 and 1.36 eV (865 and 910 nm), i.e. the main IR-RF emission and a possibly contaminating one, respectively, presumably correspond to the newly described emission peaks whose peak centres range 1.40–1.42 eV (885–874 nm) and 1.30–1.35 eV (953–917 nm), respectively.

Further investigations on the emissions neighbouring the main IR-RF peak are needed to assess their possible effects on equivalent dose (D_e) estimation for dating. In this paper, we obtain RF spectra of two K-feldspar samples of known ages and compare the D_e obtained from the different wavelength ranges associated with the discussed RF peaks. IR-RF D_e values have previously been obtained for these samples (Table 1): (i) a modern sample yielded a D_e value not consistent with zero, suggesting a residual dose of ~20 Gy for IR-RF measurements and (ii) a sample of geologic age yielded a finite De value (i.e., not saturated), suggesting the onset of field-saturation occurs earlier than expected, at ~1000–1500 Gy (Murari et al., 2021a). A better understanding of the spectroscopic composition of the IR-RF signal might help elucidate the reported luminescence behaviours.

2. Material and methods

2.1. Sample selection and preparation

Two samples of different geological provenances were selected to test for differences in their luminescence behaviour (Table 1) and were prepared following standard procedures to extract the K-feldspar fraction, as detailed elsewhere (Murari et al., 2021a). Sample Gi326 originates from a Triassic sandstone near Bayreuth, Germany and has an expected dose of ~500 000 Gy, (Murari et al., 2021a). Sample Gi361 (also called LUM1225 in Murari et al. (2021a) and CUD 1-E in Kunz et al. (2010)) was taken from a modern coastal dune in Cuddalore, south-east India. This sample was prepared by the Leibniz Institute for Applied Geophysics (LIAG Hannover, Germany) and its age was determined by quartz optically stimulated luminescence (OSL) to be 61 ± 5 a (D_e = 0.10 ± 0.01 Gy; Kunz et al., 2010).

Medium-sized aliquots (~4 mm) each containing hundreds of coarse grains of 90–200 µm (Gi326) or 150–200 µm (Gi361) in diameter were mounted on stainless steel cups with silicone oil.

2.2. Mineralogical characterisation

An automated system of quantitative evaluation of minerals by scanning electron microscopy (QEMSCAN©; FEI Company) was used for mineralogical characterization of the samples at the CSIRO Australian Minerals Research Centre, Western Australia. Samples were prepared following previously published methods (Meyer et al., 2013), which included impregnating the grains in resin, polishing and carbon-coating. Mineralogical maps were created by (i) scanning an electron beam over the resin block and detecting the resulting X-ray emissions with energy-dispersive detectors and (ii) determining the chemical composition of each pixel by comparing the X-ray spectrum with a database of characteristic spectra of known mineral phases using a peak integral method.

Both samples are dominated by K-feldspar (88.8–96.2 wt%), with small proportions of other minerals, e.g., albite, quartz or muscovite, as detailed in Table 2.

2.3. Instrumental setup for luminescence measurements

RF measurements were performed on a lexsyg research device (Freiberg Instruments GmbH; Richter et al., 2013) containing an annular beta source (90Sr/90Y; Richter et al., 2012) calibrated with a standard quartz sample. We assume an uncertainty of 5% for this calibration. RF was detected by a Hamamatsu H7421-50 photomultiplier tube (PMT) filtered through band-pass filters centred at 850 nm (FWHM = 40 nm) or 710 nm (FWHM = 10 nm), respectively named Chroma D850/40 and FB 710/10. Alternatively, RF was filtered through a FELH 500 nm long pass filter and then transmitted through a fibre optic light guide to a built-in spectrometer constituted by an Andor Shamrock 163 Czerny-Turner type spectrograph containing a diffraction grating with 300 lines/mm and a blaze wavelength of 500 nm coupled to an Andor Newton DU920P back-illuminated charge-coupled device (CCD) camera. Pixel positions were wavelength-calibrated using a third-degree polynomial fit of 10 fluorescent light emission peaks between 588 and 976 nm. The wavelength-dependent spectrometer efficiency was calibrated according to the efficiencies declared by the manufacturers of the long pass filter, the fibre optic attachment lens, the CCD camera, the spectrograph mirror coatings and grating. RF was always measured at 70°C, following Frouin et al. (2017). Each measured channel corresponds to 10 and 19 s integration time for detection with the PMT and the spectrometer, respectively. Samples were bleached using the built-in "solar simulator" with emissions in the following wavelengths using the power output shown in brackets: 365 nm (9 mW), 462 nm (55 mW), 525 nm (47 mW), 590 nm (32 mW), 625 nm (100 mW), and 850 nm (84 mW). The relative intensities of the different LEDs correspond to those suggested by Frouin et al. (2015).

2.4. Spectral data analysis

Instrumental background was removed from RF spectra by subtracting at each pixel position the mean counts (n = 2500 channels) obtained in the measurement of an empty disc. No dose dependent signal was observed in the background measurement. Outliers caused by cosmic rays or other background radiation (visible as sharp peaks in the spectra) were removed using two procedures. First, the R function apply_CosmicRayRemoval() (Kreutzer, 2020) contained in the Luminescence package (Kreutzer et al., 2021) was applied iteratively a total of six times, repeating the option 'smooth' (a running median of length 3 following Tukey (1977)) along the time axis and then the wavelength axis. Second, we iteratively removed data points whose first derivative on the wavelength axis (calculated using the absolute difference quotient) exceeded a threshold of 10% of the 90% quantile of the entire RF measurement. Removed data points were replaced by the mean of data points on either side. The efficiency correction was applied using the R function apply_EfficiencyCorrection() (Kreutzer and Friedrich, 2021). Conversion of the wavelength to energy scale occurred through the R function convert_Wavelength2Energy() (Kreutzer, 2021a).

3. PMT decay shapes

The RF emissions of both samples were characterised using PMT measurements in two wavelength ranges to capture the main IR-RF emission and a possibly contaminating red RF emission, respectively: (i) ~825–875 nm using an 850/40 nm band-pass filter and (ii) ~700–720 nm using a 710/10 nm band-pass filter. RF was measured after bleaching previously measured aliquots for 25 000 s with the "solar simulator" and then waiting an additional 2 h. The IR-RF emissions of the two samples follow similar dose responses up to 4000 Gy regenerative dose, though that of sample Gi326 decreases faster, as shown in Figure 1a–c. In contrast, the emissions around 710 nm differ starkly between the samples, with an initial signal decay for sample Gi326 up to ~300 Gy and then a saturating signal increase until the end of the measurement at ~4000 Gy (Figure 1e). Sample Gi361 only displays the saturating increasing signal (Figure 1d).

The behaviour observed for sample Gi326 can be explained by the superposition of two different emissions. From the PMT measurements alone, we cannot assess what emission causes the decreasing signal at ~710 nm, as it could originate from an emission at this wavelength (both emissions of relatively similar brightness) or from the tail of a brighter emission at higher or lower wavelengths. Spectroscopic measurements might elucidate this issue.

4. RF spectra

RF spectra were obtained for three aliquots of each sample following a standard protocol (Table 3). After background and cosmic ray removal (see section 2.4), the energy spectrum of each channel was fitted with a sum of four Gaussian functions between 1.31 eV (950 nm) and 1.91 eV (650 nm), to focus on the red-IR range and avoid the etaloning effect at high wavelengths. Sums of between two and six Gaussians were also tested, but four yielded the best visual fit with the measured data and was the model with fewest components which gave an R2 value of >0.98 for both samples. Fitting occurred in two steps. First, the function was fitted to each spectrum of the regenerative dose measurement allowing for variation of the peak centres, widths and amplitudes. The resulting median peak centres and widths were then fixed for each aliquot (i.e., 4x peak centres and widths for each regenerative dose measurement). In the next step, the spectrum of each channel of the natural and of the regenerative dose measurements was fitted allowing only for variation of the peak amplitude. Representative fit examples are shown for both samples in Figure 2a–b. Overall, the fits lead to low fit residuals, but we note that for sample Gi326, and to a lesser extent for Gi361, there is a slight dose-dependency between 0 and ~750 Gy (Figure 2c–d).

In addition to the four fitted peaks, there also appears to be an IR-RF emission centred at ~1.25–1.30 eV (950–990 nm). However, due to the high noise in this wavelength range and to the limit of our calibration being at 976 nm, we did not attempt to fit a function to it. Should there indeed be a peak in this wavelength range, its tail would overlap with those of the other two IR peaks.

The two-step fitting procedure ensures all channels of a measurement have the same peak centres and widths, allowing dose response curves to be built from the amplitudes of each peak and ensuring that the natural and regenerative dose response curves are directly comparable. However, by applying the median peak parameters of the regenerative dose curve to fit the natural dose one, this method is blind to possible sensitivity changes between the natural and regenerative dose response curves. Therefore, as a reliability check, the natural dose measurement should also be fitted allowing for variation of the peak centres, widths and amplitudes and the results compared to the peak parameters obtained from the regenerative dose spectra. Here, variations of 0–6 nm and 0.00–0.01 nm were observed for the median peak centres and widths, respectively, suggesting there was no significant change between the RF emissions in the natural and regenerative measurements.

Representative dose response curve examples are shown for one aliquot of each sample in Figure 3a–b. As expected, the signals from the two IR-RF peaks (light blue and navy blue curves) decrease with increasing dose for both samples. However, whereas the amplitudes from both red RF peaks of sample Gi361 increase with dose, those of sample Gi326 are more complicated. The peak amplitude at 795 nm (brown curve; regenerative dose) has an initial decrease until a few hundred Gy, after which the signal appears saturated, and the peak amplitude at 680 nm (red curve; regenerative dose) follows a similar pattern as observed in the PMT measurement at ~710 nm (see Figure 1e), with an initial decay and then a rise. This suggests that the 4-peak model is insufficient to describe this spectrum, possibly because of the presence of strongly overlapping additional peaks with opposite behaviour with respect to dose. It should, thus, only be regarded as a rough approximation for this sample.

The signal proportions of the individual emissions relative to the total signal in the wavelength range that would be measured using a PMT and an 850/40 nm filter (considering their wavelength-dependent efficiencies) are shown in Figure 3c–d. Since the different emissions have different behaviours with dose, the relative proportion of the red emissions at 680–800 nm increases in relation to the IR emissions with increasing dose, but even after 4000 Gy regenerative dose, they correspond to at most 4–5% of the total signal. Due to the low filter transmission and PMT efficiency at high wavelengths, the 917–919 nm peak has only a minute contribution of ~0.1%. Additionally, we observe only small differences of <0.5% relative signal contribution of the different peaks between the natural and regenerative dose measurements of sample Gi361 (Figure 3c, bottom), indicating insignificant wavelength-dependent sensitivity changes; since this is a modern sample, the dose ranges should be directly comparable between natural and regenerative dose measurements.

5. Influence on IR-RF D_e

Despite the small proportion of the neighbouring RF emissions relative to the main IR-RF peak, the former might lead to inaccuracies in D_e estimation, especially due to the changing signal contribution at different doses. We investigated this possibility by calculating the D_e values in two ways: either using the amplitudes of the fitted functions or from the total signal integration at different wavelengths.

5.1. Spectrum fitting

We obtained D_e values for the two fitted IR peaks of each of three aliquots per sample by sliding the natural dose curves onto the corresponding regenerative dose curves obtained in section 4

horizontally and vertically ('slide' method) to account for sensitivity changes using the R function analyse_IRSAR.RF() (Kreutzer, 2021b). An example of D_e estimation is shown in Figure 4 for the main IR-RF peak of one aliquot of sample Gi326; example dose response curves are shown in Figure 3a–b for all peaks.

Whereas the long natural dose measurement of 30 000 s (equivalent to ~2000 Gy) was useful in section 4 to compare the emission contributions between the natural and regenerative dose curves, using the full natural dose measurement length for D_e estimation would limit the obtainable D_e to ~2300 Gy, since during the sliding algorithm the natural dose curve cannot slide further than the end of the regenerative dose curve (i.e., after sliding, no "tail" of the natural dose curve is allowed). Only the portion of the natural dose signal measured between 200 s and 10 000 s (~13 and 670 Gy) was used to assess the fit in the sliding algorithm. Removal of the initial channels, as suggested by Buylaert et al. (2012), avoids the effect of a possible 'initial rise' common in IR-RF signals (summarised in Murari et al., 2021b) and removal of the final channels increases the upper dating limit to ~3700 Gy. The remaining channels not used for fitting can still be used to visually assess the fit (shown in grey in Figure 4).

Considering the three aliquots of sample Gi361, the higher-wavelength IR emission (919 nm) leads to a weighted mean D_e value of 46.2 ± 10.9 Gy, whereas the lower wavelength IR emission (876–879 nm) leads to a weighted mean D_e of -11.1 ± 2.3 Gy. Negative IR-RF D_e values have been reported previously and are explained by an incomplete bleaching with the "solar simulator" relative to the natural bleaching (Buylaert et al., 2012). Interestingly, previous PMT-D_e estimates obtained for this sample in eight laboratories range 15.1 ± 1.4 to 59.5 ± 8.1 Gy (Murari et al., 2021a), suggesting the PMT system, in which ~95% of the transmitted signal comes from 830–875 nm, might yield an average of the two overlapping IR peaks with different bleachabilities.

For sample Gi326, the two IR-RF peaks yield indistinguishable (at 1σ) weighted mean D_e values of 1583.4 ± 376.8 Gy (917 nm) and 1458.9 ± 165.7 Gy (874–875 nm). These are slightly higher than the PMT-D_e previously obtained in Giessen of 1259 ± 179 Gy, but compatible with the IR-RF D_e range obtained for this sample by seven other laboratories of 1081 ± 117 to 1539 ± 438 Gy (Murari et al., 2021a). As can be seen in Figure 4, the portion of the natural dose curve not used for fitting has a substantially worse agreement with the regenerative dose curve than the portion used for fitting. We also tested using the whole natural curve in the fitting procedure, which led to a good fit for the whole curve and increased the resulting D_e to 1644.2 ± 224.2 Gy (917 nm) and 1725.7 ± 143.7 Gy (874–875 nm). To maintain comparability with the work of Murari et al. (2021a), who only measured the initial 10 000 s

(~750 Gy at time of measurement), here and in the next section we focus on the results using the shorter measurement range, but point out that these results suggest sensitivity changes occur during the natural dose measurement for both IR peaks.

We also calculated the proportion of saturation of the natural signal of both IR peaks for all aliquots. We first normalised the RF dose response curve of each peak, so that the beginning and end of the regenerative dose curve were set to zero and 100%, respectively, representing the fully-bleached and saturated states. We defined the zero-saturation signal intensity as the maximum RF signal value within the first 100 channels of the regenerative dose measurement, since the first measurement channel isn't necessarily the highest, due to, e.g., a possible 'initial rise' of the signal. The signal intensity at full-saturation was chosen to be the median RF signal of the 100 last channels of the regenerative dose measurement to account for the measurement uncertainty of individual channels.

The relative saturation of each channel of the natural dose measurement was then determined for each peak by normalising the sensitivity-corrected natural dose curve (i.e., considering the vertical offset that leads to the best fit in the 'slide' method) with the same parameters as the corresponding regenerative dose curve. The final relative saturation of the natural signal (dashed grey line in Figure 4) was then defined as the minimum relative saturation percentage in the first 15 channels of the natural measurement to account for the possibility of an 'initial rise'.

The IR-RF signals of the two samples were expected to be at opposite extremes in terms of signal saturation. Indeed, the mean saturation of the natural RF signal of Gi326 was 86% for both IR peaks (average of three aliquots for each peak) and that of Gi361 was 8% (917 nm peak) and -7% (876–879 nm peak), following the pattern described for the D_e values estimated for these peaks.

5.2. Total signal integration

The continuous measurements of the spectrometer also allow for investigations into signal saturation and D_e calculation to be made across the whole measured wavelength range without any of the assumptions necessary for fitting regarding the number and nature of emissions (Figure 5).

The natural signal saturation was calculated for each wavelength using the same normalisation as described in section 5.1 for wavelengths with decreasing RF dose response curves. In the case of wavelengths with increasing RF dose response curves, the minimum RF signal (within the first 100 channels) and the median RF signal (within the last 100 channels)

were set to 0 and 100% saturation, respectively. Examples of dose response curves are given in Figure S1 for various wavelengths (saturation shown on right-hand axes).

The natural IR-RF signal saturation obtained in this manner has a similar behaviour to that estimated from spectrum fitting. At wavelengths in the range 820–920 nm the relative saturation of the natural signal of Gi361 is below (but consistent with) zero and that of Gi326 ranges ~80–90% saturation (Figure 5a–b).

We calculated weighted mean D_e values for each wavelength using the same horizontal and vertical sliding procedure as in section 5.1. At the wavelength ranges observed with a PMT and the filters typically used in lexsyg research (850/40 nm) and Risø systems (Chroma D900/100 nm; Lapp et al., 2012) (red and orange shading in Figure 5), the D_e values of samples Gi361 and Gi326 are relatively constant and similar to those obtained for the main IR peak (874–879 nm) in section 5.1. This D_e plateau region extends until ~930 nm, thus also covering the wavelength range of the second IR peak, though we note that the 874–879 nm peak still constitutes ~50% of the signal integration at this wavelength range.

Striking for both samples is a peak in D_e values at ~790 nm, which coincides with one of the fitted red emissions (note that these D_e estimations use the integrated signal and not the fitted functions). A high degree of saturation of up to 100% is also observed for both samples, indicating this wavelength range is unreliable for dating due to a small dose-dependency of the RF signal (see also Figure S1e). The tail of this high D_e 'peak' is still present in the first few nanometres of the PMT and 850/40 nm filter transmission range, especially for sample Gi326 (Figure 5d). In fact, in the laboratory comparison of Murari et al. (2021a), the only laboratory using the PMT and 900/100 nm filter (which only transmits in slightly higher wavelengths than the 850/40 nm filter; see red and orange shading in Figure 5) yielded D_e values on the lower end (but still within 1σ) of the range obtained by the other seven laboratories for both samples.

The wavelength range corresponding to the second red emission, at 680–700 nm, yields relatively low D_e values of ~350–650 Gy for the geologically old sample Gi326, in keeping with the expectation that there is a thermally unstable red emission (Trautmann et al., 1998; Krbetschek et al., 2000). The relative natural saturation at this wavelength range is consistent with zero (Figure 5b), indicating a substantial instability, but the analysis is complicated by the non-monotonic behaviour of sample Gi326 at this wavelength range (see Figure S1b, d).

6. Discussion

As in previous spectroscopic work, the main visible IR peak was best fitted by a sum of two peaks, with peak centres ranging 1.41–1.42 eV (876–879 nm) and 1.35 eV (919–921 nm) for

the three aliquots of Gi361 and ranging 1.42 eV (874–875 nm) and 1.35 eV (917–918 nm) for the three aliquots of Gi326. The values for both samples are very similar and also match well previously reported IR-RF peaks at 1.40–1.42 eV (874–885 nm) and 1.30–1.35 eV (917–953 nm) (Kumar et al., 2018; Riedesel et al., 2021). Therefore, our results also support the view that the main IR-RF peak is not centered at 865 nm but rather at 880 nm, and as a consequence the choice of band pass filter for PMT measurements should be reviewed, as one centred at 850 nm may not be optimal for detection of this IR-RF signal.

For sample Gi361, a small peak was observable in the red RF range (Figure 2a), but it was necessary to assume the presence of two peaks in this range to obtain a good fit: at 1.80–1.83 eV (676–688 nm) and at 1.59–1.60 eV (774–782 nm). For sample Gi326, there was no obvious red RF peak even at relatively high doses (see Figure 2b), but, similarly, two peaks were necessary for a reasonable fit: at 1.82–1.83 eV (678–681 nm) and at 1.56–1.57 eV (792–797 nm). Especially given the heterogeneous material in sedimentary samples, we consider the presence of multiple peaks leading to an almost linear spectrum in the red-orange range a plausible explanation. It is supported by measurements at cryogenic temperatures, which described peaks centred at 1.68 and 1.77 eV (738 and 700 nm) for one K-feldspar sample (Kumar et al., 2018). The possibility of other such small peaks in the IR cannot be ruled out and could contribute to the high background of IR-RF PMT measurements (i.e., why continued irradiation does not lead to zero RF, as shown in Figure 1c). However, high-resolution spectroscopic measurements at cryogenic temperatures would be needed to investigate this possibility, something currently not possible with our device.

The small signal proportion of the red emissions relative to the IR ones (Figure 3c–d), amounting to at most 5% of the total signal at the wavelength range measured with a conventional PMT system, suggests that they would not significantly alter the IR-RF D_e values. This view is supported by a 'D_e plateau' in the wavelengths 830–900 nm for both samples (Figure 5). However, it could theoretically be possible that other samples have different signal intensity ratios between the red and IR emissions, in which case the red emissions could potentially contribute significantly to the total signal. According to our results, contribution from the emission at ~1.56–1.59 eV (774–797 nm) would lead to overestimated IR-RF D_e values, something which has been reported for two polymineral samples with high red-RF to IR-RF ratios (Heydari et al., 2021). Use of alternative band-pass filters, such as the 900/100 nm one, should be further investigated even for samples with relatively high IR-RF signals (see section 5.2).

Unlike in OSL dating, where it has been suggested to only consider D_e values below 86% saturation as reliable (Wintle and Murray, 2006), there is no conventionally used saturation threshold in IR-RF dating. Here, the mean signal saturation in the wavelength ranges of 810–850 and 850–890 nm differs by only ~2% (88% and 86% saturation, respectively), which might appear insignificant, whereas the resulting mean D_e values differ by ~400 Gy (~1876 and 1460 Gy, respectively). Due to the density of measurements, the errors associated with D_e values remain relatively low even close to signal saturation, but the uncertainty associated with the sensitivity correction is more difficult to ascertain, so it may be useful to establish such a threshold for IR-RF dating.

7. Conclusions

Spectroscopic RF measurements of two sedimentary K-feldspar samples suggest that for these samples the influence of neighbouring RF emissions of smaller wavelength only has a small contribution to the total signal detected in conventional PMT measurements and does not lead to a change in D_e. As previously reported for one K-feldspar sediment sample (Kumar et al., 2018), we also find that the second, smaller IR emission at ~1.35 eV (917–921 nm) has a very similar dose response (see Figure 3a–b) and resulting D_e (see section 5.1) as the main IR emission at 1.41–1.42 eV (874–879 nm), so it could potentially be of interest to use a wavelength range further into the IR (<900 nm) for IR-RF measurements of samples with a higher proportion of contaminating red emission(s).

Acknowledgements

The authors were supported by the German Research Foundation (MSG and MF: DFG FU417/36-1; MF: DFG FU417/19-1). Sumiko Tsukamoto is thanked for providing sample Gi361. Peter Austin (CSIRO) is thanked for the QEMSCAN measurements. Geoff Duller and an anonymous reviewer are thanked for their constructive comments, which greatly improved this manuscript.

References

Arnold, L.J., Roberts, R.G., Galbraith, R.F., DeLong, S.B., 2009. A revised burial dose estimation procedure for optical dating of young and modern-age sediments. Quaternary Geochronology 4, 306–325. https://doi.org/10.1016/j.quageo.2009.02.017

Buylaert, J.-P., Jain, M., Murray, A.S., Thomsen, K.J., Lapp, T., 2012. IR-RF dating of sand-sized K-feldspar extracts: A test of accuracy. Radiation Measurements 47, 759–765. https://doi.org/10.1016/j.radmeas.2012.06.021

Degering, D., Krbetschek, M.R., 2007. 11. Dating of interglacial sediments by luminescence methods, in: Sirocko, F., Claussen, M., Sánchez Goñi, M.F., Litt, T. (Eds.), Developments in Quaternary Sciences, The Climate of Past Interglacials. Elsevier, pp. 157–171. https://doi.org/10.1016/S1571-0866(07)80036-4

Erfurt, G., Krbetschek, M.R., 2003. Studies on the physics of the infrared radioluminescence of potassium feldspar and on the methodology of its application to sediment dating. Radiation Measurements 37, 505–510. https://doi.org/10.1016/S1350-4487(03)00058-1

Frouin, M., Huot, S., Mercier, N., Lahaye, C., Lamothe, M., 2015. The issue of laboratory bleaching in the infrared-radiofluorescence dating method. Radiation Measurements 81, 212–217. https://doi.org/10.1016/j.radmeas.2014.12.012

Frouin, M., Huot, S., Kreutzer, S., Lahaye, C., Lamothe, M., Philippe, A., Mercier, N., 2017. An improved radiofluorescence single-aliquot regenerative dose protocol for K-feldspars. Quaternary Geochronology 38, 13–24. https://doi.org/10.1016/j.quageo.2016.11.004

Galbraith, R.F., Roberts, R.G., Laslett, G.M., Yoshida, H., Olley, J.M., 1999. Optical dating of single and multiple grains of quartz from Jinmium rock shelter, northern Australia: Part I, experimental design and statistical models. Archaeometry 41, 339–364. https://doi.org/10.1111/j.1475-4754.1999.tb00987.x

Heydari, M., Guérin, G., Zeidi, M., Conard, N.J., 2021. Bayesian luminescence dating at Ghār-e Boof, Iran, provides a new chronology for Middle and Upper Paleolithic in the southern Zagros. Journal of Human Evolution 151, 102926. https://doi.org/10.1016/j.jhevol.2020.102926

Lapp, T., Jain, M., Thomsen, K.J., Murray, A.S., Buylaert, J.-P., 2012. New luminescence measurement facilities in retrospective dosimetry. Radiation Measurements 47, 803–808. https://doi.org/10.1016/j.radmeas.2012.02.006

Krbetschek, M.R., Trautmann, T., Dietrich, A., Stolz, W., 2000. Radioluminescence dating of sediments: methodological aspects. Radiation Measurements 32, 493–498. https://doi.org/10.1016/S1350-4487(00)00122-0

Kreutzer, S., 2020. apply_CosmicRayRemoval(): Function to remove cosmic rays from an RLum.Data.Spectrum S4 class object. Function version 0.3.0. In: Kreutzer, S., Burow, C., Dietze, M., Fuchs, M.C., Schmidt, C., Fischer, M., Friedrich, J., 2020. Luminescence: Comprehensive Luminescence Dating Data Analysis. R package version 0.9.7.

Kreutzer, S., 2021a. convert_Wavelength2Energy(): Emission Spectra Conversion from Wavelength to Energy Scales. Function version 0.1.1. In: Kreutzer, S., Burow, C., Dietze, M., Fuchs, M.C., Schmidt, C., Fischer, M., Friedrich, J., Mercier, N., Philippe, A., Riedesel, S., Autzen, M., Mittelstrass, D., Gray, H.J., 2021. Luminescence: Comprehensive Luminescence Dating Data Analysis. R package version 0.9.15. https://CRAN.R-project.org/package=Luminescence.

Kreutzer, S., 2021b. analyse_IRSAR.RF(): Analyse IRSAR RF measurements. Function version 0.7.8. In: Kreutzer, S., Burow, C., Dietze, M., Fuchs, M.C., Schmidt, C., Fischer, M., Friedrich, J., Mercier, N., Philippe, A., Riedesel, S., Autzen, M., Mittelstrass, D., Gray, H.J., 2021. Luminescence: Comprehensive Luminescence Dating Data Analysis. R package version 0.9.15. https://CRAN.R-project.org/package=Luminescence.

Kreutzer, S., Burow, C., Dietze, M., Fuchs, M.C., Schmidt, C., Fischer, M., Friedrich, J., Mercier, N., Riedesel, S., Autzen, M., Mittelstraß, D., Gray, H.J., 2021. Luminescence: Comprehensive Luminescence Dating Data Analysis. R package version 0.9.11. https://CRAN.R-project.org/package=Luminescence

Kreutzer, S., Duval, M., Bartz, M., Bertran, P., Bosq, M., Eynaud, F., Verdin, F., Mercier, N., 2018. Deciphering long-term coastal dynamics using IR-RF and ESR dating: a case study from Médoc, south-west France. Quaternary Geochronology 48, 108–120. https://doi.org/10.1016/j.quageo.2018.09.005

Kreutzer, S., Friedrich, J., 2021. apply_EfficiencyCorrection(): Function to apply spectral efficiency correction to RLum.Data.Spectrum S4 class objects. Function version 0.2.0. In: Kreutzer, S., Burow, C., Dietze, M., Fuchs, M.C., Schmidt, C., Fischer, M., Friedrich, J., Mercier, N., Philippe, A., Riedesel, S., Autzen, M., Mittelstrass, D., Gray, H.J., 2021. Luminescence: Comprehensive Luminescence Dating Data Analysis. R package version 0.9.15. https://CRAN.R-project.org/package=Luminescence.

Kumar, R., Kook, M., Murray, A.S., Jain, M., 2018. Towards direct measurement of electrons in metastable states in K-feldspar: Do infrared-photoluminescence and radioluminescence probe the same trap? Radiation Measurements 120, 7–13. https://doi.org/10.1016/j.radmeas.2018.06.018

Kunz, A., Frechen, M., Ramesh, R., Urban, B., 2010. Luminescence dating of late Holocene dunes showing remnants of early settlement in Cuddalore and evidence of monsoon activity in south east India. Quaternary International 222, 194–208. https://doi.org/10.1016/j.quaint.2009.10.042

Meyer, M.C., Austin, P., Tropper, P., 2013. Quantitative evaluation of mineral grains using automated SEM–EDS analysis and its application potential in optically stimulated luminescence dating. Radiation Measurements 58, 1–11. https://doi.org/10.1016/j.radmeas.2013.07.004

Murari, M.K., Kreutzer, S., Frouin, M., Friedrich, J., Lauer, T., Klasen, N., Schmidt, C., Tsukamoto, S., Richter, D., Mercier, N., Fuchs, M., 2021a. IR-RF of K-feldspar: An interlaboratory comparison. Geochronometria 48, 105–120. https://doi.org/10.2478/geochr-2021-0007

Murari, M.K., Kreutzer, S., King, G., Frouin, M., Tsukamoto, S., Schmidt, C., Lauer, T., Klasen, N., Richter, D., Friedrich, J., Mercier, N., Fuchs, M., 2021b. Infrared radiofluorescence (IR-RF) dating: A review. Quaternary Geochronology 64, 101155. https://doi.org/10.1016/j.quageo.2021.101155

Richter, D., Richter, A., Dornich, K., 2013. LEXSYG - A new system for luminescence research. Geochronometria 40, 220–228. https://doi.org/10.2478/s13386-013-0110-0

Riedesel, S., Kumar, R., Duller, G.A.T., Roberts, H.M., Bell, A.M.T., Jain, M., 2021. Site-selective characterisation of electron trapping centres in relation to chemistry, structural state and mineral phases present in single crystal alkali feldspars. J. Phys. D: Appl. Phys. 54, 385107. https://doi.org/10.1088/1361-6463/ac10d7

Schilles, T., 2002. Die Infrarot-Radiolumineszenz von Feldspäten und ihr Einsatz in der Lumineszenzdatierung. PhD thesis, Ruprecht-Karls-Universität Heidelberg, Germany.

Trautmann, T., Krbetschek, M.R., Dietrich, A., Stolz, W., 1998. Investigations of feldspar radioluminescence: potential for a new dating technique. Radiation Measurements 29, 421–425. https://doi.org/10.1016/S1350-4487(98)00012-2

Trautmann, T., Dietrich, A., Stolz, W., Krbetschek, M.R., 1999a. Radioluminescence Dating: A New Tool for Quaternary Geology and Archaeology. Naturwissenschaften 86, 441–444. https://doi.org/10.1007/s001140050649

Trautmann, T., Krbetschek, M.R., Dietrich, A., Stolz, W., 1999b. Feldspar radioluminescence: a new dating method and its physical background. Journal of Luminescence 85, 45–58. https://doi.org/10.1016/S0022-2313(99)00152-0

Trautmann, T., Krbetschek, M.R., Dietrich, A., Stolz, W., 2000. The basic principle of radioluminescence dating and a localized transition model. Radiation Measurements 32, 487–492. https://doi.org/10.1016/S1350-4487(00)00119-0

Tukey, J.W., 1977. Exploratory data analysis. Addison-Wesley, Reading, MA.

Wagner, G.A., Krbetschek, M., Degering, D., Bahain, J.-J., Shao, Q., Falguères, C., Voinchet, P., Dolo, J.-M., Garcia, T., Rightmire, G.P., 2010. Radiometric dating of the type-site for *Homo heidelbergensis* at Mauer, Germany. PNAS 107, 19726–19730. https://doi.org/10.1073/pnas.1012722107

Figures and Tables

Table 1: *Sample details.*

Code	Size (µm)	Location	Context	IR-RF D_e (Gy)[a]	Reference
Gi361	150–200	Cuddalore, SE India	Modern coastal dune	18.6 ± 9.7	Murari et al. (2021a) as LUM1225; Kunz et al. (2010) as CUD 1-E
Gi326	90–200	Bayreuth, Germany	Triassic sandstone	1259 ± 179	Murari et al. (2021a)

[a] Previous IR-RF D_e estimates obtained in Giessen using the same luminescence reader as in this work equipped with a PMT and 850 nm (FWHM = 40 nm) interference filter (Murari et al., 2021a).

Table 2: *Mineralogical sample composition determined by QEMSCAN. The classifications 'alkali feldspar' and 'plagioclase' refer to a mineral composition between the endmembers in a ternary system.*

Mineral	**Gi361 (wt%)**	**Gi326 (wt%)**
Feldspar series	97.7	94.1
Endmember K-feldspar	96.2	88.8
Alkali feldspar	0.2	1.1
Endmember albite	1.1	4.2
Plagioclase	0.2	0.0
Quartz	0.8	3.6
Muscovite	0.3	1.2
Biotite/Phlogopite	0.2	0.0
Kaolinite	0.1	0.2
Pyroxene	0.0	0.7
Fe Aluminosilicate	0.8	0.0
Fe Silicate	0.0	0.0
Amphibole	0.0	0.0
Rutile/Anatase	0.0	0.1
Ilmenite	0.0	0.0
Ti-mineral trap	0.0	0.1
Others	0.0	0.0

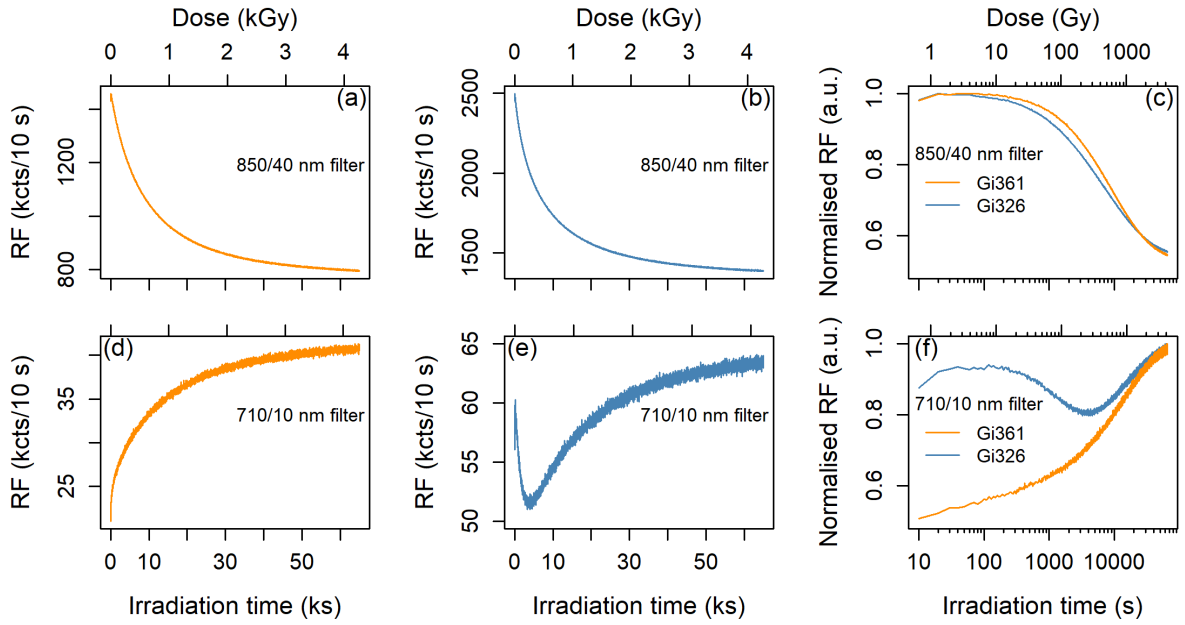

Figure 1: *Regenerative dose response curves obtained using a PMT and either (a, b, c) an 850/40 nm or (d, e, f) a 710/10 nm filter for two samples: (a, d) Gi361 (orange) and (b, e) Gi326 (blue). (c, f) show the same data as in previous plots on a logarithmic time scale and normalised to the highest signal intensity. Different aliquots were used for each measurement.*

Table 3: Radiofluorescence (RF) measurement protocol. RF was detected with a spectrometer.

Step	Treatment	Purpose
1	Preheat at 70°C for 900 s	Stabilise temperature
2	RF at 70°C for 30 000 s	Obtain natural dose curve
3	"Solar simulator" bleaching for 25 000 s	Fully remove signal
4	Pause for 2 h	Reduce phosphorescence
5	RF at 70°C for 65 000 s	Obtain regenerative dose curve

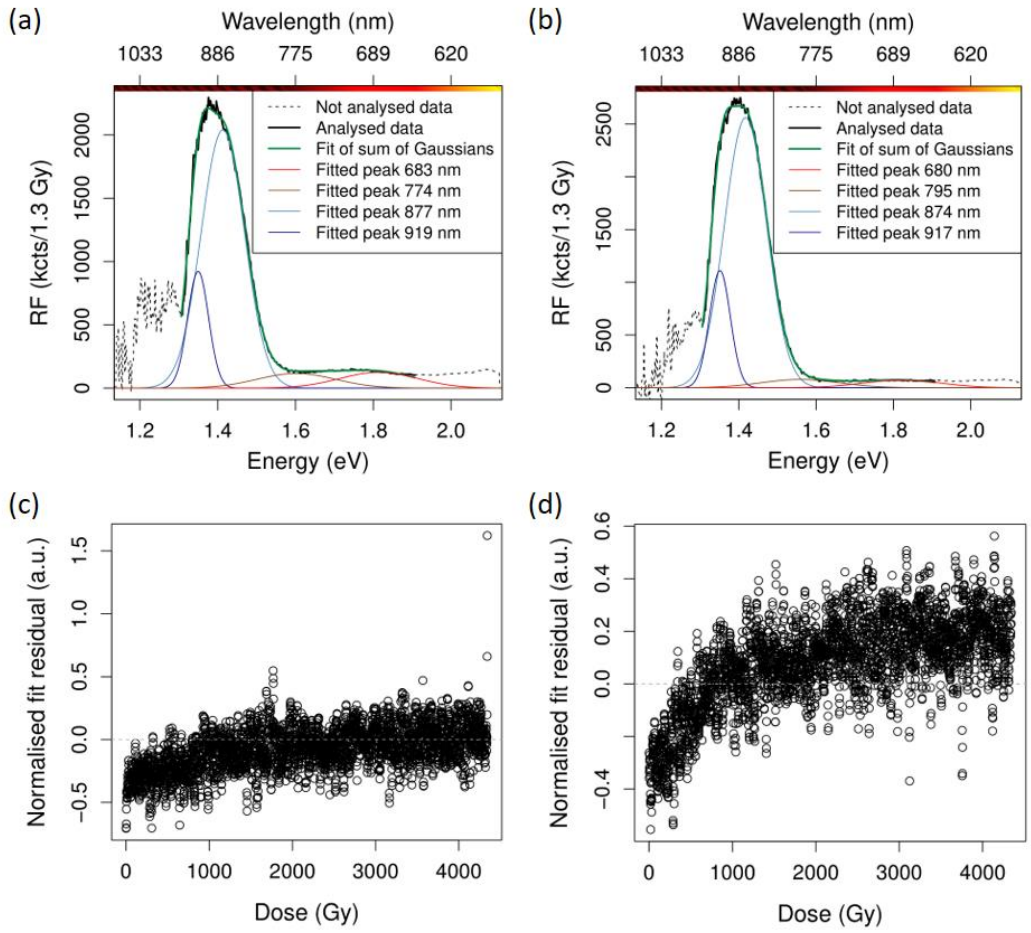

Figure 2: *RF spectra of samples (a) Gi361 and (b) Gi326 taken after 1000 Gy regenerative dose, fitted with a sum of four Gaussian functions (green curve) from 1.31 eV (950 nm) to 1.91 eV (650 nm). The fit residuals across the whole regenerative dose measurement series (3250 spectra), normalised to the maximum RF signal of each channel, are shown in (c) for Gi361 and in (d) for Gi326.*

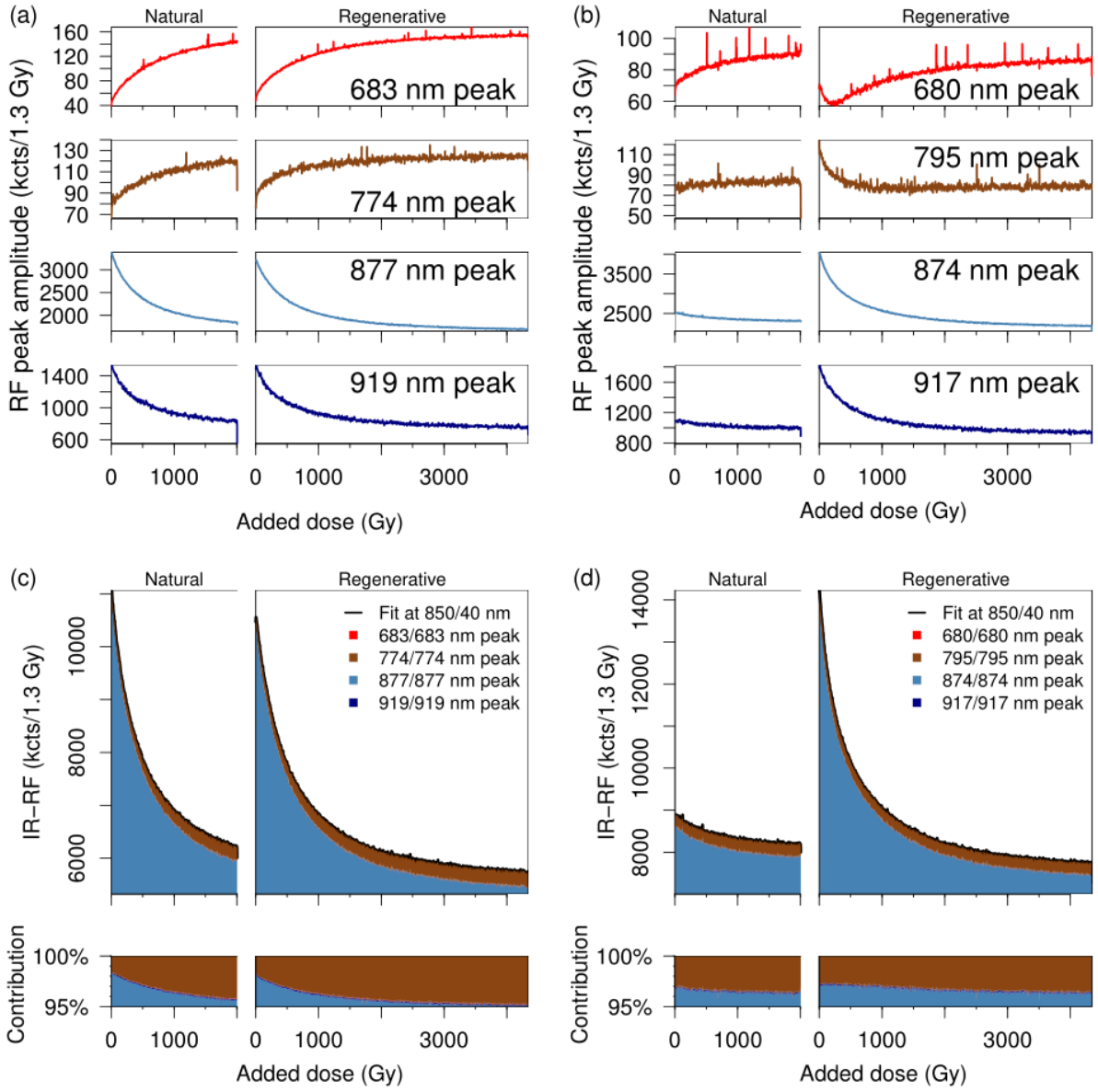

Figure 3: *(a, b) Natural and regenerative dose response curves of the amplitudes of the four fitted Gaussian functions of one representative aliquot of (a) Gi361 and (b) Gi326. The peak centre wavelengths are stated for each peak. (c, d) The signal proportion from natural and regenerative doses of the four functions to the total signal that would be transmitted in the conventionally measured wavelength range with a PMT and an 850/40 nm filter is shown in absolute values (main plots) and in percentages (bottom plots) for samples (c) Gi361 and (d) Gi326.*

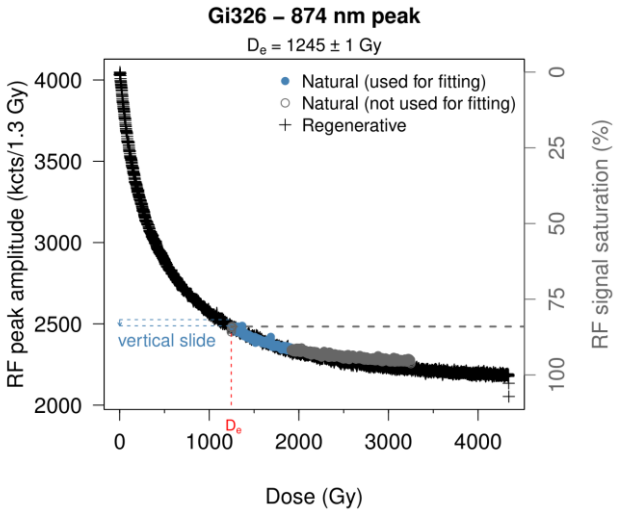

Figure 4: *Spectroscopic RF D_e estimation using the 874 nm peak amplitude of one aliquot of sample Gi326. The D_e (indicated by the red dashed line) is obtained by sliding the natural dose measurements (blue circles) on the regenerative dose measurements (black crosses) until an optimal fit between the curves is reached. The extent of vertical slide for sensitivity change correction is shown as a blue arrow between dashed lines. The right-hand y-axis shows the signal intensity relative to the saturation of the regenerative dose measurement. The dashed grey line indicates the initial saturation of the natural signal.*

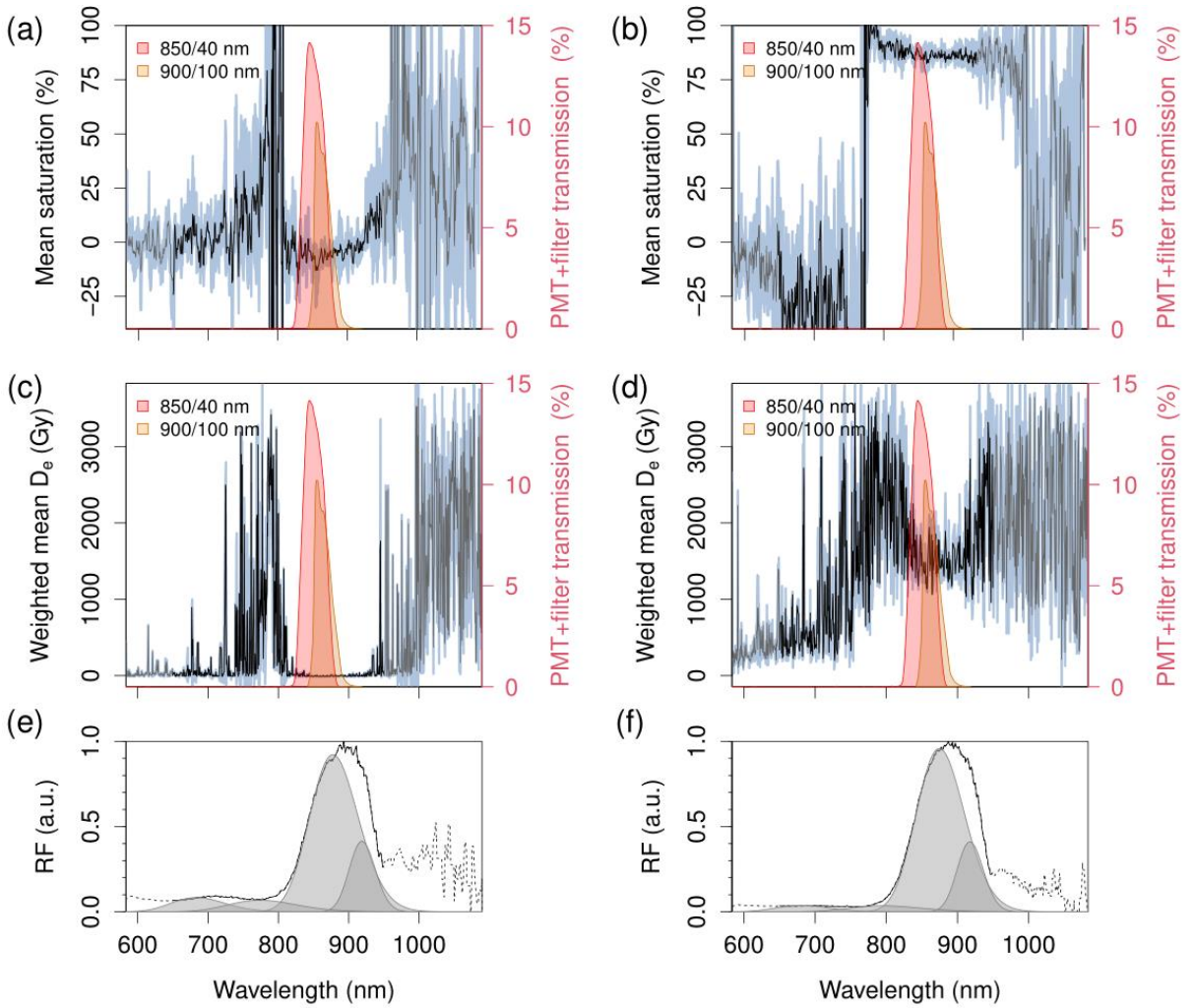

Figure 5: *Wavelength-resolved RF natural signal saturation and D_e for samples (a, c, e) Gi361 and (b, d, f) Gi326. (a,b) Proportion of the initial natural RF signal (after vertical sliding) relative to the regenerative signal saturation. The average of three aliquots per sample is shown as black and grey lines for reliable and unreliable wavelength ranges, respectively. The blue shaded regions indicate the range of values obtained for the three aliquots. (c, d) D_e values were obtained via horizontal and vertical sliding of the natural curve onto the regenerative curve at each wavelength. The blue shaded regions indicate the standard errors. The wavelength range transmitted in a conventional PMT and either 850/40 or 900/100 nm filter combination is shown shaded red and orange, respectively (right-hand y-axis). For comparison, (e,f) show the emission spectra of one aliquot of each sample at 4333 Gy regenerative dose normalised to the highest intensity as well as the four fitted Gaussian functions (shaded grey).*